

## PHYSICS AND RADIATION BIOLOGY

## Performance Evaluation of a Positron Tomograph Designed for Brain Imaging

Edward J. Hoffman, Michael E. Phelps, and Sung-Cheng Huang

*University of California, Los Angeles, California*

The NeuroECAT, a multiplane positron tomograph for imaging the brain, was characterized in terms of both quantitative performance and image quality. The tomograph has four modes of operation, defined by the placement of interplane septa and shadow shields. Each mode was fully characterized by measurement of image resolution, axial resolution, resolution uniformity, scatter, accidentals, and deadtime. Each measurement was performed with scattering media simulating the human head, and resolutions were obtained from images processed with reconstruction techniques actually used in patient imaging. The results for the most frequent mode of operation are: image resolution  $9.8 \pm 0.2$  mm (FWHM), axial resolution  $12.4 \pm 0.4$  mm, and scatter  $8.1\% \pm 0.6$ . At a count rate of 10,000 cps per image plane, accidentals are 9% and the deadtime 3%. Accidentals are measured and subtracted in hardware, and corrections for deadtime loss are calculated from the on-line measurement of triple-coincidence events. Scatter is estimated from the scan data and subtracted in software. Image quality is demonstrated by phantom studies and by the patient images obtained with [F-18] fluorodeoxyglucose and carbon-11 monoxide. The FDG images show clear delineation of the convolutions of the cortical ribbon, internal gray nuclei, internal and external capsules, and other substructures of the brain. The carbon monoxide images, in addition to visualizing the large vessels, clearly show the blood volumes of the cortex, the Sylvian fissure, and the circle of Willis.

J Nucl Med 24: 245-257, 1983

The NeuroECAT is a multiple-plane positron emission computerized tomography (PCT) system designed to do quantitative cross-sectional imaging of the brain (1,2). The instrument incorporates the previous developments in coincidence electronics and data handling designed for the ECAT (3,4) whole-body PCT system.

A PCT system dedicated to brain imaging will have higher sensitivity per detector than a comparable whole-body system of larger diameter. However, smaller-diameter systems tend to have poorer resolution uniformity (both image and axial), higher scatter frac-

tion, and worse accidental-to-true coincidence ratios (1,5-9). These factors are primary considerations in choice of system diameters and designs of interplane shielding. In order to optimize the quantitative capability of such systems, trade off between competing performance parameters are often required. When possible, these choices should be decided in favor of the parameter that does not lend itself to corrections after data collection. For instance, uniformity of axial resolution as a function of position in the field of view (FOV) can be optimized for interplane images at a cost in additional scatter and accidental events in the data (5). Scatter and accidental coincidences can be measured or estimated and removed from data, whereas it may not be possible to compensate for large nonuniformities of axial resolution.

The purpose of this paper is to present a comprehen-

---

Received April 15, 1982; revision accepted Nov. 29, 1982.

For reprints contact: Edward J. Hoffman, PhD, Div. of Biophysics, Dept. of Radiological Sciences, UCLA School of Medicine, Los Angeles, CA 90024.

sive evaluation of the performance of the NeuroECAT. The rationale and details of many of the test procedures have already been presented (3,6,9).

#### SYSTEM DESCRIPTION

The PCT (1,2) has three octagonal detector planes each with 88 bismuth germanate (BGO) detectors. The system diameter is 66 cm, with a 32-mm center-to-center distance between detector planes. Each detector is 17 mm wide (10.5 mm with shadow shields), 27 mm high (axial dimension), and 29 mm deep. The coincidence resolving time is 20 nsec, and accidental coincidences are measured in hardware and either subtracted or recorded for subsequent software subtraction (4). The system uses a scan (2.8 mm steps) and rotate (1.9 deg) data-collection scheme.

The system has a unique interplane septum design (1,2,10), which is diagrammed in Fig. 1. In the instrument the septa are either in place or retracted on all sides of the head, and the shadow shields are independent of the septa. When septa are in place, the system has reduced scatter and accidentals and slightly better axial

resolution, but interplane data are not collected. When septa are retracted, the system efficiency increases by a factor of three due to increases in amount of activity viewed per plane and the use of interplane data. Since scatter and accidental coincidences are greater in this mode, the option is typically chosen for low-flux-rate imaging. The two positions of the septa and shields define the four modes of operation that were tested.

#### MATERIALS AND METHODS

**Resolution.** Image and axial resolutions were measured with a phantom consisting of a Plexiglas cylinder 20 cm in diameter by 12.5 cm deep, with a pattern of 1-mm holes on vertical, horizontal, and  $\pm 45^\circ$  radial lines (9). Either Cu-64 or F-18 (maximum beta energies 653 and 634 keV, respectively (11) was used in resolution measurements to minimize effect of positron range on resolution (12,13).

For measurements of image resolution, holes containing positron emitter were at least 36 mm apart to minimize overlap of line spread functions (LSFs) in the image. A pattern of ten holes was chosen as a representative sampling of a distribution of positron emitter 18 cm in diameter (9). The phantom was imaged four times with and without shadow shields, a geometric attenuation correction was applied (14), and images reconstructed on a 100 by 100 grid of 2 mm and 2 mm pixels. The reconstruction used the filtered back-projection technique, with the ramp filter (15), the Shepp filter (16) in its standard form (high), and the Shepp filter with the cutoff frequency reduced by either a factor of two (medium) or three (low). Horizontal and vertical histograms through the maximum of each source in the image were used to form LSFs for determinations of image resolution. Each LSF was fitted with a Gaussian by least-squares fitting techniques to determine the FWHM (17). The full width at tenth maximum (FWTM) was determined by interpolation between data points at tenth maximum of each LSF. The above measurement was repeated without shadow shields for a scan mode in which 5.55-mm linear spatial sampling is used.

In order to estimate resolution losses due to the linear and angular sampling and the reconstruction process alone, a line source was simulated by Gaussians with FWHMs equal to the intrinsic detector pair resolutions of the PCT. The Gaussian shape was sampled at a 2.8 mm sampling interval and a  $2.5^\circ$  angular interval, with the Ramp filter (15) used in the reconstruction.

The axial resolution was measured as a function of distance from the center of the FOV with the same resolution phantom. However, the phantom was rotated  $90^\circ$  to align the source parallel to the image plane, and only one hole contained positron emitter for each measurement, all of which were made through the thickest dimension of the phantom. The measurement was made

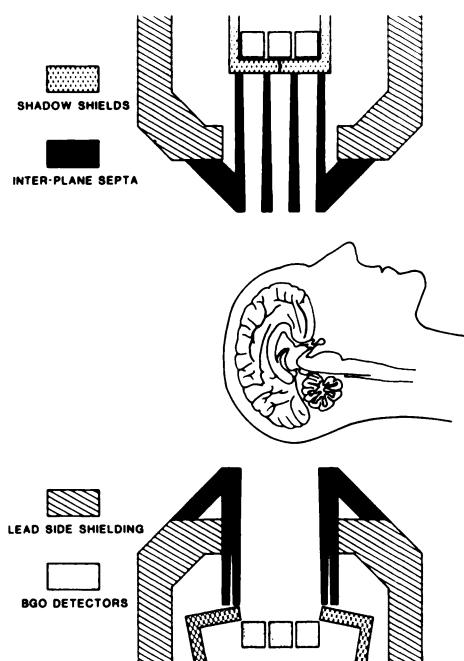


**Fig 1.** Diagram of septa and shadow-shield design of NeuroECAT. When septa are in place (top), gap in the lead near the patient is 20 mm and it increases to 27 mm at detector surface. This configuration makes full use of crystal for each slice, while reducing accidental and scatter coincidences. No interplane data are collected in this configuration. When septa are retracted (bottom), the interplane data can be collected with minimum distortion of axial slice thickness. In this configuration, system's efficiency is increased by a factor of 2.8 with less rejection of scatter and accidental coincidences. This mode of operation is designed for those cases in which only a small amount of activity is in FOV either because of low availability of tracer, or low extraction into brain. Brain, septa, and detector sizes and positions are in correct proportion.

by stepping the patient bed through the gantry in 2-mm increments using the rectilinear scan option of the system. Axial resolutions were obtained with septa for a single plane slice, and as both single plane and interplane slices with septa retracted. The LSFs were fitted with Gaussians to estimate the FWHM, and the FWTM was obtained by interpolation between data points near tenth maximum.

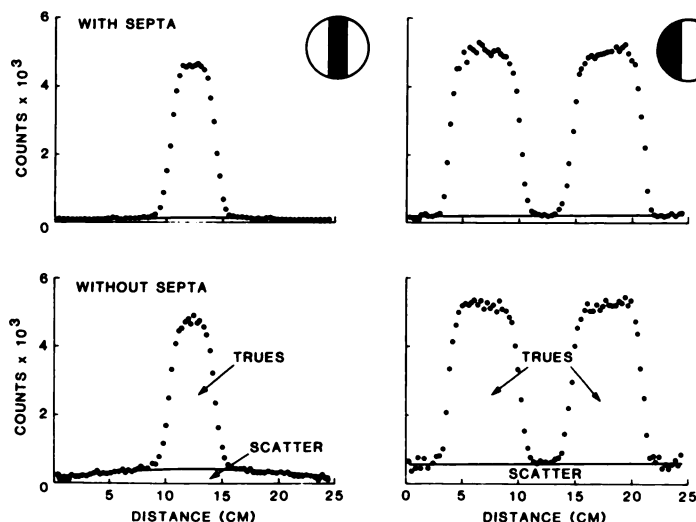
**Sensitivity.** System sensitivity was measured with cylinders of uniformly dispersed positron activity, 20 and 17.8 cm in diameter (3,9). In each determination, accidental coincidences were measured and subtracted from total coincidences, and the scatter fraction was subtracted from the total to give only true unscattered coincidences as the measure of sensitivity. The absolute activity in the cylinder was measured with a calibrated Ge(Li) spectrometer, and the sensitivity is expressed as counts per microcurie-per-ml of pure positron emitter.

The effect of differences in the distribution of geometric efficiency between circular and octagonal detector configurations was estimated by computer simulation (17). This assumed identical detectors (10 mm FWHM Gaussian-shaped line spread functions), system diameter (66 cm), detector spacing (22.2 mm center-to-center), and linear sampling distances (2.8 mm) for both geometries. Each detector pair is assumed to have identical efficiency with six additional detectors in the circle to fill out the geometry. The simulation was performed for uniform cylinders of positron emitter 12, 14, 16, 18, 20, 22, and 24 cm in diameter. Three types of scanners were simulated: (a) the octagonal geometry of the NeuroECAT, in which the geometry and scanning pattern gives 96 angles of 88 data points each, a pattern of relative efficiency of 11 for the central eight points within each angle, and a decrease of one unit of efficiency for each additional four points from the center down to one unit of efficiency at the edge of the field of view; (b) a circular geometry with uniform linear sampling,

2.775-mm sampling distance, no gantry motion, and constant sensitivity from point to point on each scan profile (physically, this system cannot exist); and c) a circular geometry that uses a wobbling motion to improve linear sampling with a wobble diameter equal to one detector width (18) and data binned in channels 2.775 mm wide, in proportion to the fraction of time the individual detector pairs would spend traversing the bin (This gives a repeating pattern of relative efficiencies of 2.86, 1.28, 1.07, 1.0, 1.0, 1.07, 1.28, and 2.86 every 22.2 mm on each scan profile.) In each case scan profiles were calculated with appropriate uniform or nonuniform sensitivity, and data were scaled to give the correct number of counts of "raw" data (one million counts for the octagon as the reference level). These data sets are equivalent to the data measured by each of these tomographs before any corrections are made for nonuniformity or attenuation. Poisson noise was added to the scan profiles and corrections for nonuniformities in the sensitivity distribution were applied to the data. The profiles were corrected for attenuation, and images were reconstructed with the standard Shepp filter (16).

**Scatter.** Scatter was measured with Plexiglas containers 17.8 cm in diameter and 3, 10, and 20 cm long. The cylinders were divided longitudinally into three compartments by walls 1 mm thick: one central compartment, 5 cm wide, running the length of the cylinder, and two identical lateral chambers (Fig. 2). Each compartment can be filled independently. In the scatter measurement, one or two of the compartments can be filled with positron emitter and the other(s) filled with water. The phantom is scanned and data profiles at the angle with the highest object-to-scatter contrast (Fig. 2) are used to estimate the scatter fraction. Data lying more than one FWHM outside the physical limits of the region containing activity are essentially pure scatter coincidences. These data are fitted, with polynomials to estimate scatter across the whole scan profile. The

**FIG 2.** Examples of data used in determining scatter fraction. Phantom configurations are diagrammed to right of upper plots. The dark areas correspond to regions filled with activity. The data correspond to views along long axis of central chamber. Solid line through the lower part of data (scatter) is a second-order polynomial fit to data lying outside the physical limits of object; integral area of this curve over whole FOV is scatter. Upper curves were obtained with shadow shields and septa in place; lower curves were obtained with shadow shields and septa retracted. Accidental coincidences have already been subtracted.



measurement is performed for various combinations of compartments, and measurements are combined to give the equivalent of scatter for a uniform cylinder.

**Accidental coincidences.** Accidental fractions were measured with a 17.8 cm diameter by 20 cm long uniform cylinder of C-11 or N-13. The NeuroECAT measures the accidentals by delayed coincidence (4) and accidentals as well as total coincidence rates are available from the tomograph. Fifty to 70 mCi were put in the cylinder and accidental fractions were measured as the radionuclide decayed.

**Deadtime.** Characteristics of the system due to deadtime were studied by reanalyzing the data for accidentals fraction and measuring the discrepancy between known physical decay rates and apparent decay rates as measured by the tomograph. In addition, triple-coincidence rates (which are encoded as an error and totaled by the data-collection electronics) were also measured as a function of count rate. A triple coincidence is usually between a valid true event and an unrelated event, an ambiguous data address is generated and the true event is lost from the data. The triple coincidence is the largest single source of lost counts by the data-collection electronics.

**Image quality.** Images of complex phantoms and patients were made to assess the system as an imaging device. Resolution was assessed with the multiple-line-source phantom described by Derenzo (19). To assess the impact of scatter in various scan modes, images were made of a bar phantom consisting of a cylinder (diam 19.2 cm) with Plexiglas bars that were 6, 9, 12, 15, and 18 mm wide, with interspaces of 6, 12, 18, and 18 mm (Fig. 3).

Normal volunteers were imaged with [F-18] fluoro-deoxyglucose (FDG) (20) and red blood cells labeled with carbon-11 monoxide ( $^{11}\text{CO}$ ) to provide examples of in vivo image quality. The FDG images are obtained with 10-mCi injections and 15-min scans per set of 3

images with septa and shadow shields. The  $^{11}\text{CO}$  blood-volume images were obtained by administering 20 mCi of  $^{11}\text{CO}$  by inhalation, and 10-min scans per set of three images with septa and shadow shields. The low-resolution filter was employed in the reconstruction of the volunteer images.

## RESULTS

**Image resolution.** Measurements of the image resolution are summarized in Table 1. Standard deviations of the FWHM and FWTM are calculated from the distribution of values taken from 80 individual LSFs from vertical and horizontal histograms through the resolution phantom images. The range is given as the best and worst resolution observed in a data set, and the differences in these two values were about twice the standard deviations. The FWHMs of the computer-simulated resolution measurements were 7.8 and 10.2 mm, with and without shadow shields respectively, for images reconstructed with the ramp filter.

**Axial resolution.** In Fig. 4, LSFs from measurements of axial resolution are plotted as a function of position in the FOV for each septal configuration.

**Sensitivity.** Results of sensitivity measurements are summarized in Table 2. The sensitivity is given for both cylinders of uniform activity, 20 cm and 17.8 cm in diameter. The accidentals were measured and the scatter estimated, and these backgrounds were subtracted from the total coincidence count rate. The 17.8 cm diameter was chosen because it was the diameter of off-the-shelf plastic tubing with cross-sectional area closest to that of the typical head in our clinical series. This choice of an appropriate diameter is of primary importance in evaluating scatter and accidental coincidences.

The computer-simulated uniform cylinder images were evaluated by determining the standard deviation of the mean pixel values for a 10-cm diam. region of in-

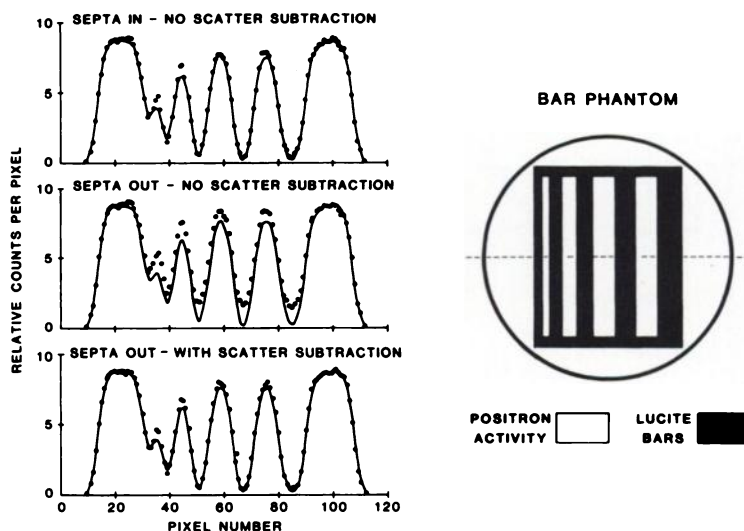


**FIG. 3.** Diagram of bar phantom and histograms through bar-phantom image taken under several conditions. Histograms correspond to dashed line in phantom diagram. Bars are 6, 9, 12, 15, and 18 mm wide, spaced at 6, 12, 18, and 18 mm, respectively. Solid line in each plot is a histogram obtained from image made with septa and shields and scatter subtraction. The upper plot illustrates the effect of scatter subtraction in that case. Lower two plots show scatter and residual scatter in images taken without septa (center) but without and with scatter subtraction (bottom).

TABLE 1. IMAGE RESOLUTION

Shadow shields	Sampling distance (MM)	Filter	Resolution (MM) FWHM $\pm$ SD	Range (MM)		FWTM (MM)
				Low	High	
In	2.775	Ramp	8.2 $\pm$ .2	7.8– 8.6		15.2 $\pm$ .4
In	2.775	High	8.4 $\pm$ .2	8.1– 8.8		15.6 $\pm$ .4
In	2.775	Medium	9.1 $\pm$ .2	8.8– 9.5		16.9 $\pm$ .4
In	2.775	Low	9.8 $\pm$ .2	9.4–10.2		18.2 $\pm$ .5
Out	2.775	Ramp	10.4 $\pm$ .4	9.9–11.2		18.8 $\pm$ .5
Out	2.775	High	10.6 $\pm$ .3	10.1–11.3		19.2 $\pm$ .6
Out	2.775	Medium	11.1 $\pm$ .3	10.7–11.8		20.3 $\pm$ .5
Out	2.775	Low	11.7 $\pm$ .3	11.2–12.2		21.4 $\pm$ .5
Out	5.55	Ramp	12.1 $\pm$ .6	11.3–13.6		22.3 $\pm$ 1.4
Out	5.55	High	12.1 $\pm$ .6	11.3–13.6		22.3 $\pm$ 1.9
Out	5.55	Medium	14.1 $\pm$ .8	13.3–15.4		25.7 $\pm$ 1.1
Out	5.55	Low	15.6 $\pm$ .5	15.6–17.5		29.4 $\pm$ 1.1

terest in the center of each image. The effect of increasing the sensitivity of a PCT system, while maintaining the same resolution, is a reduction in the random noise in the image. A measure of this noise is the standard deviation of the mean pixel value of an image of a uniform distribution of activity. A technique that reduces the standard deviation without loss of resolution effectively increases the sensitivity of the scanner. Since the reduction in the standard deviation of the pixel values is inversely proportional to the square root of the number of accumulated events, a comparison of the square of the standard deviations of the pixel values for the simulated uniform cylinder images gives a measure of the relative effective efficiency per event of the two systems. In Fig. 5 the ratio (circle/octagon) of the effective system efficiencies is plotted as a function of cylinder diameter. The straight line at 1.0 is the octagon compared to itself and the dashed line is the gross efficiency of the circular

geometry relative to the octagon for a cylinder with no attenuation. The plotted curves show the effective efficiencies of the two simulated circular systems, relative to the octagon, when attenuation is included. Each effective efficiency is derived from multiple simulations of each case and the error bars indicate the random variation of the simulation.

**Scatter.** Results of the scatter measurements are summarized in Table 3. Measurements for the phantom 10 cm long have error estimates because the data were obtained from three different combinations of four different phantom configurations: with emitter in one side chamber, in the middle chamber, in the middle plus one side chamber, and in both side chambers. Data were combined to give the equivalent of the image and scatter of a uniform cylinder, and the error is the range of values from the three combinations of the data. Since the error is small, scatter was determined only from combinations

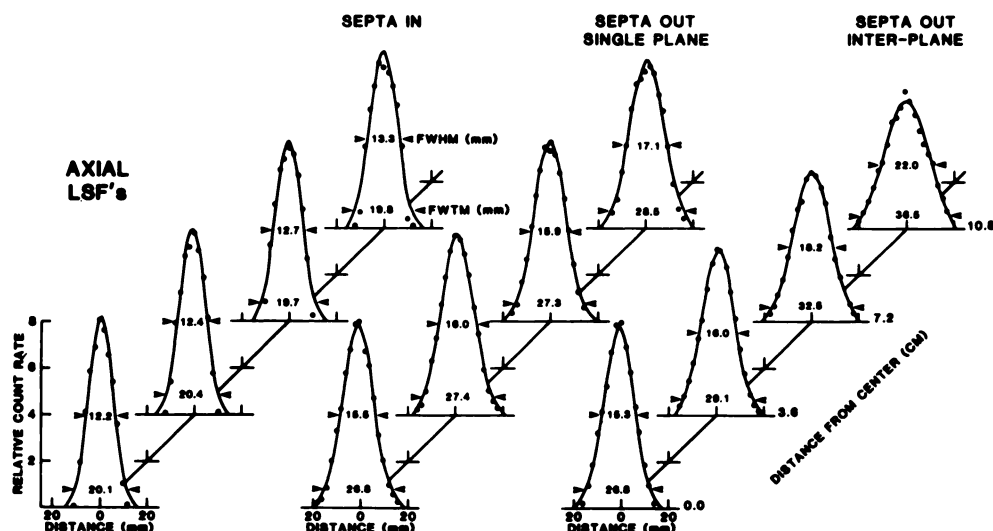


FIG. 4. Axial line spread functions as a function of distance from center of FOV for both configurations of septa. Solid lines are least-squares fit of Gaussian to data.

TABLE 2. SENSITIVITY

System configuration		Sensitivity*			
Septa	Shields	Cylinder 20 cm diam.		Cylinder 17.8 cm diam.	
		One plane	System	One plane	System
In	In	13,100	39,400	15,800	47,300
In	Out	23,300	70,000	27,300	82,000
Out	In	17,200	120,500	18,800	132,000
Out	Out	27,900	195,600	32,100	225,000

\* Sensitivity is given in cps ( $\mu\text{Ci/ml}$ )<sup>-1</sup>. In all sensitivity measurements accidental coincidences have been measured and subtracted, and scatter coincidences have been estimated (see text) and subtracted.

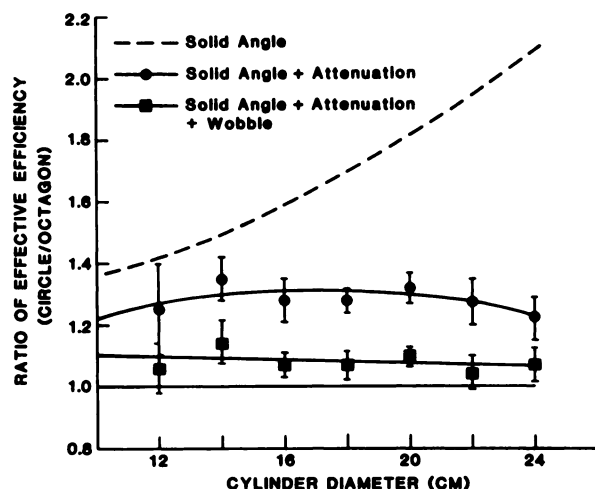


FIG. 5. Plot of ratio of effective efficiency of circular to octagonal detector geometries having identical detectors, detector spacing, and sampling distance. Solid line at 1.0 is line of identity for ratio of circle to octagon as a function of cylinder diameter when no attenuation is assumed in simulation calculation. Data plotted as round points show the effective efficiency after the attenuation in the object and spatial distribution of sensitivity are taken into account. Data plotted as square points include the effect of data collection nonuniformities, which are inherent in sampling of the wobble motion.

of data from phantoms with two side chambers filled and with the middle chamber filled for the 3- and 20-cm-long phantoms.

**Accidental coincidences.** Ratios of accidental to true

coincidence are plotted in Fig. 6, for all septa and shadow-shield configurations against the true coincidence count rate. Note that the point of reference for the measurement is the true coincidence rate.

**Deadtime.** In Fig. 7, percent deadtime loss is plotted against true coincidence rate for each septa- and shadow-shield configuration. Triple coincidences were also measured and the relationship between the deadtime losses and the triple coincidences is given by the following equation

$$\text{DTL} = 1.58 (\text{TC}) + 0.101 (\text{TC})^{3/2}, \quad (1)$$

where DTL is the deadtime loss in counts per second, and TC is the triple-coincidence rate. The constants are the averages of constants obtained by least-squares fits of deadtime loss as a function of TC for all four scanner configurations. The deadtime loss, as calculated by Eq. (1), was used as a deadtime correction for the data involved in the determination of the accidental-to-true coincidence ratios. The gross count rate correction equation is

TRUE COUNTS =

$$\text{Observed True events} + \text{DTL} \times T, \quad (2)$$

where T is the data collection time in seconds. The corrected data were then fit to a single exponential by a least squares fitting routine and the resultant half time agreed with the physical decay time of the isotope to within better than 0.5% for all scanner configurations. In

TABLE 3. SCATTER

Septa		Scatter fraction as percent of true coincidences		
		Axial thickness of the phantom		
	Shadow shields	3 cm	10 cm	20 cm
In	In	7.6	8.1 $\pm$ 0.6	8.7
In	Out	8.6	10.1 $\pm$ 0.7	10.5
Out	In	8.7	23.8 $\pm$ 1.5	27.6
Out	Out	10.6	29.4 $\pm$ 1.0	40.8

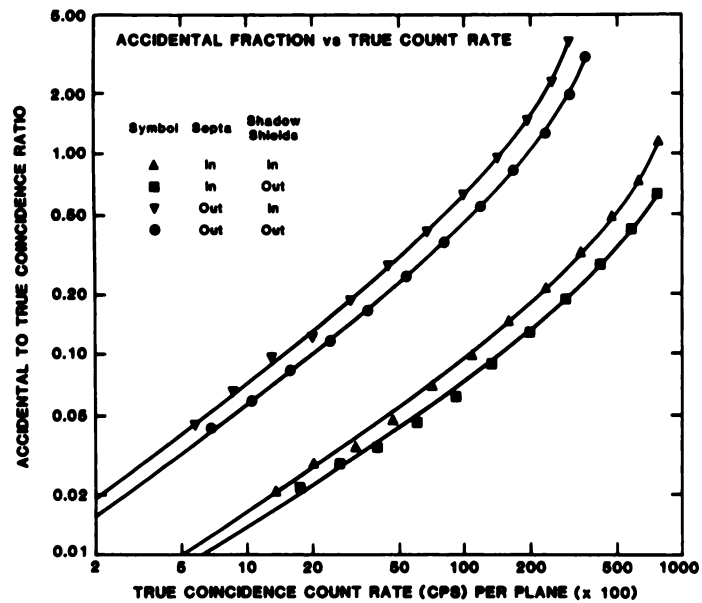


FIG. 6. Plot of accidental-to-true coincidence ratio as a function of true coincidence rate for all septa and shadow-shield configurations. Data were collected with a uniform cylinder of positron emitter 17.8 cm in diameter by 20 cm long.

practice the deadtime correction is applied to the data as a correction factor

$$\text{Correction Factor} = \frac{\text{True Coincidences} + \text{DTL} \times T}{\text{True Coincidences}} \quad (3)$$

**Image quality.** Images of the Derenzo phantom are shown in Fig. 8. They are derived from the same set of data, each processed with one of the different reconstruction filters used for Table 1. The data were taken with both the shadow shields and septa in place.

The bar phantom was imaged with shadow shields in place and with septa in and septa out. A simple estimate of scatter was made by averaging data lying outside the object in each scan profile. This constant value was subtracted from each data point in that scan profile be-

fore reconstruction. In Fig. 3, histograms through the image data, perpendicular to the long axis of the bars, have been plotted for several conditions. The solid line in each plot is the histogram through the image obtained with septa and scatter subtraction. While this procedure underestimates the scatter in the center slightly, the resultant image is a good approximation of an image with no scatter and is used as a point of reference for the other examples. The top plot in Fig. 3 shows the effect of the scatter with septa in place. The middle plot shows the increase in scatter with septa retracted, and with bottom plot shows the effectiveness of the relatively simple scatter correction on the relatively large amount of scatter detected when septa are retracted.

Figures 9-11 provide examples of patient images for a more subjective evaluation of the system. The FDG

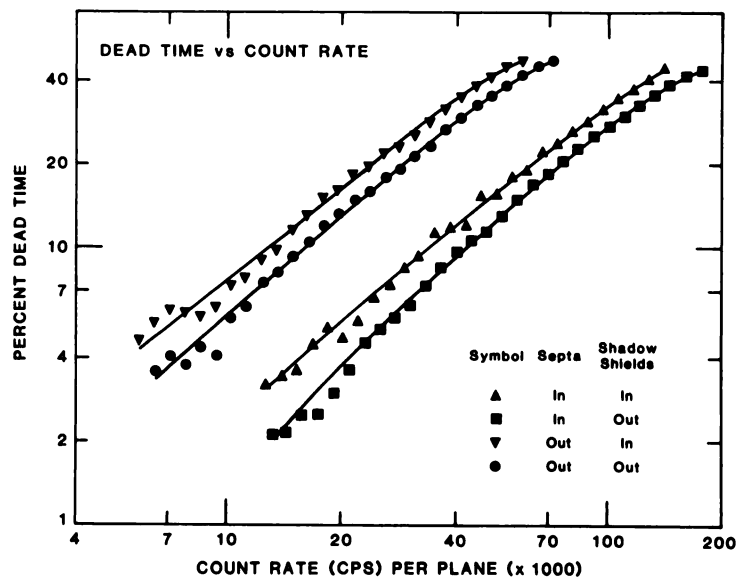
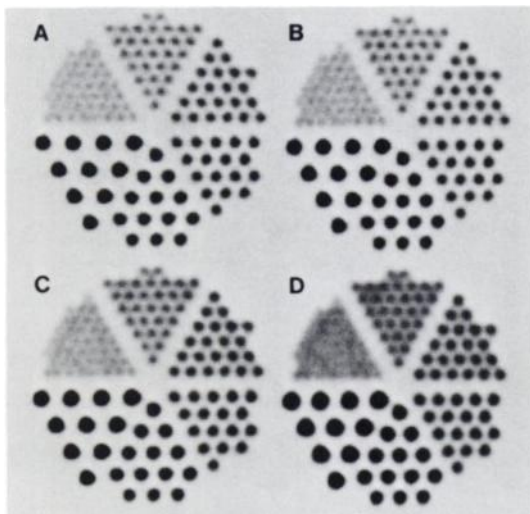


FIG. 7. Plot of percent deadtime loss as a function of true coincidence count rate for all septa and shadow shield configurations. Data were collected from uniform cylinder of positron emitter 17.8 cm diameter by 20 cm long.





**FIG. 8.** Images of Derenzo phantom derived from same data set by processing with four different reconstruction filters used in Table 1. Data were collected with septa and shadow shield in place. Hole spacings, smallest to largest, are 10, 12, 14, 16, 20, and 25 mm, respectively. Diameter of each hole is one fourth of interhole spacing.

images in Fig. 9 are derived from a single set of data, which have been processed by each of the reconstruction filters used from Table 1. The FDG images in Fig. 10 illustrate tomographic delineation of structures throughout the brain and the images at the lower right are rectilinear scans of the brain, used to identify levels that are to be scanned. The  $^{11}\text{CO}$  blood-volume scan in Fig. 11 delineates such anatomical features as the Sylvian fissure, cerebral cortex, and circle of Willis; these are usually difficult to discern because of their low object contrast.

#### DISCUSSION

**Resolution.** The purpose of resolution measurements is to evaluate the hardware of the PCT system and the capability of the system in a clinical imaging environment. The intrinsic resolution—7.4 mm FWHM with shields (9) and 9.8 mm FWHM without shields (1)—and the resolution measured with the ramp filter (15), provide an evaluation of the system's hardware. The resolution measured with the ramp filter provides a measure of the total effect of the many small factors that degrade resolution relative to the intrinsic resolution—such as sampling distance (linear and angular), pixel size, small errors in positioning of data (mechanical), integer round-off, resolution nonuniformities, etc. Results of the simulated resolution measurement (7.8 mm with and 10.2 mm without shields), when compared with the image resolution with the ramp filter, indicate that the average loss of resolution, due to sources of error other than the reconstruction filter, pixel size, and sampling distance, is 0.4 mm (5%) with shields and 0.2 mm (2%) without shields.

For an extended, complex object and sufficient accumulated events, the PCT is capable of providing an image resolution of 8.2 mm FWHM (Fig. 8A). In clinical studies, which are typically statistics-limited, the highest-resolution filter may not be practical. In Fig. 9 the effect of four different filters is seen for the same cross section of an FDG image. The image in A (ramp filter) has obvious random mottle, while the image in D (low-resolution filter) has no visible mottle. Each image in Fig. 9 is interpretable and can be analyzed quantitatively. Figures 9A and B, however, require a practiced eye and would require averaging over more pixels to give reliable quantitation than the images in Figs. 9C and D. The images in Fig. 9 contain four million counts, which is above average for a patient image since these generally contain between one and five million counts. When only one million counts are collected per image, the ramp and high-resolution filters produce images that are too mottled to be reliably interpreted.

One design goal was to provide a PCT system with good uniformity of resolution. In Table 1 it can be seen that the full range of measured resolutions for any filter or shadow-shield configuration is within  $\pm 6\%$  of the mean resolution when the linear sampling is 2.8 mm. The images of the Derenzo phantom in Fig. 8 demonstrate that this resolution variation is imperceptible in the image. The 5.6-mm sampling is used when a short scan time is required, and since this sampling distance satisfies only the minimum sampling requirements for the reconstruction, the resolution uniformity is poorer (21).

**Axial resolution.** Previous work in this laboratory (10,5) indicates that serious nonuniformities in axial

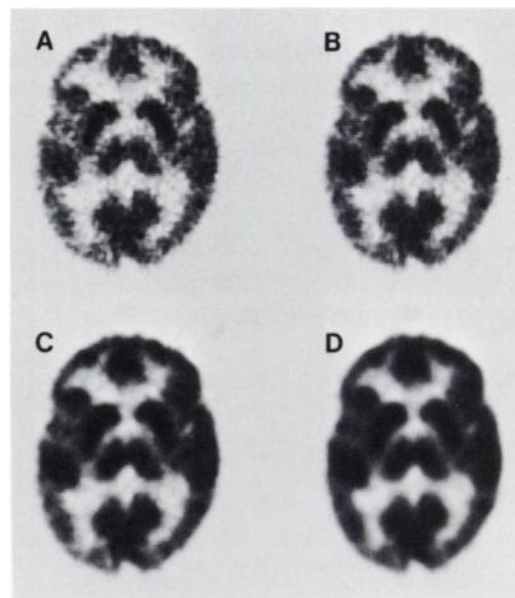


**FIG. 9.** FDG images, all from same patient data but reconstructed with four different reconstruction filters used in Table 1. Image was made with septa and shadow shields in place, and contains 4 million events.



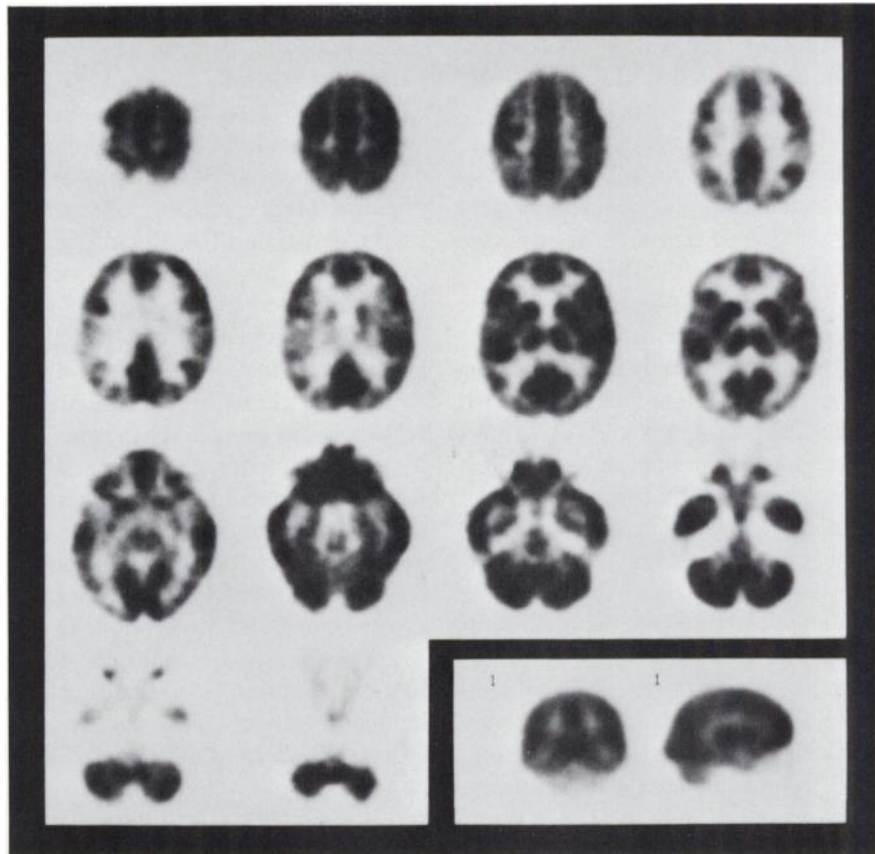


**FIG 10.** FDG images of whole brain. Images to lower right are rectilinear scans, which can be used to position patient automatically. In tomographic images, convolutions of cortical ribbon are clearly delineated; so are subcortical structures including thalamus, caudate, and globus pallidus-putamen complex. Both posterior and anterior limbs of internal capsule are visualized, and basal ganglia are distinct and separate from overlying insular cortex. Also visualized are brain stem and substructures of the cerebellum, such as cerebellar cortex, vermis, and dentate nucleus.

resolution result if system diameters are too small and interplane images are obtained with septa in place. The worst distortions occur in interplane measurements

(factors of 2 to 3 in FWHM from center to edge of FOV). The LSFs in Fig. 4 show that a 66-cm system diameter with retraction of septa for interplane mea-

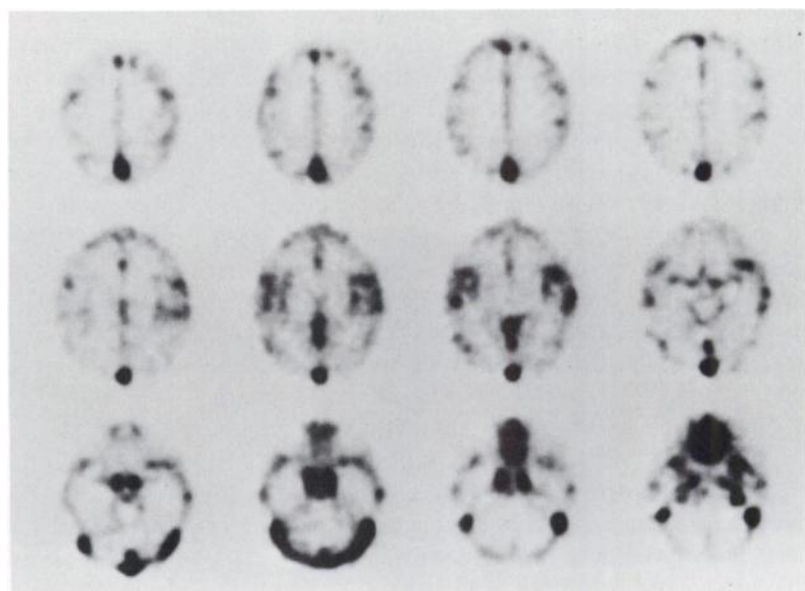


**FIG 11.** Images of carboxy(C-11) hemoglobin as blood volume in brain. In addition to indicating large blood vessels and circle of Willis, image clearly shows higher blood content of cortex, particularly near sylvian fissure.

surements, generally alleviates the problem. The variation is larger than desirable, but it is no worse than the variation measured for a single-plane configuration with a 45-cm system diameter (22).

**Sensitivity.** In measuring sensitivity, care was taken to subtract contributions to total count rate that were not true unscattered coincidence events. Accidentals were measured and subtracted, and scattered events were estimated and also subtracted. Inclusion of accidental and/or scattered events in the sensitivity is inappropriate in that: (a) it includes, as part of the true signal, events that are clearly background; (b) not only are these events not part of the true signal, the fact that they are collected with the data degrades the true signal; and (c) systems that are poorly designed will seem to have better sensitivity than well-designed systems that have minimized scatter and accidentals.

The primary effect of higher sensitivity in PCT is reduction of random noise in the image. Any technique that reduces random noise can be evaluated in terms of effective efficiency or sensitivity. The concept of effective efficiency has been used (23,24) to describe how accidental or scatter coincidences degrade image quality by effectively reducing efficiency. Investigators of time-of-flight (TOF) for PCT implicitly use the same concept when they describe improvement due to TOF in terms of higher efficiency (25,26).

When the error propagation in a PCT image of a uniform cylinder of activity in a nonattenuating medium was examined, it was found that noise for pixels in the center of the image was 25% greater than for those at the edge of the image (27). In addition, for cross sections the size of a human head, attenuation reduces count rates through the center head to less than count rates at the edge (23). As previously discussed by Phelps et al. (3,28), a PCT system with its highest sensitivity in the center of the cross section could partially compensate for greater noise at the center of the image.

For circular systems equivalent, in every way except shape, to the octagon, gross efficiency will always be significantly higher as indicated by the dashed line in Fig. 5. However, the sensitivity with circular geometry is nearly constant across a scan profile, whereas the octagonal geometry is at a maximum at the center and decreases towards the edge. Simulations of uniform cylinders provide an estimate of how well the sensitivity distribution can compensate for the lower gross efficiency of the octagon, after attenuation and reconstruction are included in the analysis. In Fig. 6, it can be seen that the circular geometry without wobble has an effective efficiency about 25% higher than the octagon for all cylinder sizes, compared with the 35 to 120% predicted by the gross efficiency. If a wobble (18) is included in the simulation, the advantage of the circle over the octagon is reduced to less than 10%.

When comparisons of the sensitivity of PCT systems

are made, the gross sensitivity does not always give the measure of the signal-to-noise ratio that is implied by such a comparison.

**Scatter.** Scatter measurements made with the 10-cm-long phantom provide the best estimate of the scatter environment of an FDG brain scan (Table 3). The 3-cm phantom gives a measure of scatter originating in the image plane, and the 20-cm phantom is essentially a worst-case infinite-length phantom. The small difference in scatter observed with septa for longer phantoms, relative to the 3 cm phantom, demonstrates the effectiveness of septa in reducing out-of-plane scatter.

The histograms in Fig. 3 demonstrate the impact of scatter on the image. When septa are used and scatter is not subtracted, there is a small discrepancy with the scatter-subtracted histogram. When septa are not used and scatter is not subtracted, the discrepancy with the scatter-subtracted histogram becomes significant. There is a 10–15% overestimate of counts for peak values near image center, and an error of the same magnitude but larger percentage for the lowest values in the histograms. In an FDG brain scan, the effect of imaging without septa and without scatter subtraction would be to overestimate FDG concentrations in central gray structures by 10–15%, and white-matter values by 30–45%. However, the simple scatter-subtraction technique (constant value for each scan profile) used in processing the bar-phantom data removed most of the systematic error due to scatter.

The simple scatter-subtraction technique used on the bar-phantom data was also applied to the data used in the scatter measurement (Fig. 2). The amount of scatter estimated by the constant-scatter-background technique was 78% of the scatter estimate obtained by a polynomial fit of scatter background with septa and was 73% of that without septa. The technique leaves a residual background of 2–3% with septa and 6–8% without septa.

In Fig. 2 scatter is seen outside the physical limits of the object in the scan profile. This scatter is suppressed in an image (Fig. 3) by two factors. 1. The scatter outside the object is essentially constant and since the integral value of the reconstruction filter is zero, the convolution of the filter with a constant is also zero. 2. The magnitude of the counts within the object is increased by an average factor of 4 by the attenuation correction, whereas the data outside the object are unchanged.

**Accidentals.** Although the accidental coincidence fraction plotted against the true coincidence rate is given in Fig. 6, one must know count rates in typical studies to appreciate their significance. The most common scan in our clinic is the FDG brain scan at 45 min after injection of a 10-mCi dose. Typical count rates range from 4000 cps and 4% accidentals with both septa and shields in place to 10,000 cps and 7% accidentals with septa and without shields. If septa are retracted, accidentals range from 28% (22% of total counts) to 47% (32% of total

counts). The percent of totals is noted because accidentals are commonly quoted as percent of total count rate. The most demanding study is the flow study, using 0-15-labeled water as tracer, in which count rates peak at 50,000 cps, giving 34% accidentals (25% of totals) without shadow shields with septa in place.

The accidentals fraction at a given count rate with and without shields should be inversely proportional to the efficiencies of the two modes, assuming the change in geometry is the only consideration (24). The accidentals fraction with shields should be about 1.8 times the fraction without shields. The ratio, which is about 1.25 (Fig. 6), is smaller because the shields provide better shielding from off-plane activity and partially shield exposed parts of the detectors from some of the activity in the image plane.

**Deadtime.** Typical deadtime corrections for the above studies are less than 2% for the FDG study with septa, 4-6% for the FDG study without septa, and 10% for the 0-15 water study with septa.

In the PCT, the signals are multiplexed into eight timing signals, each representing one side of the octagon, and after a coincidence has been established, the address of the two detectors involved is determined. The coincidence strobe pulse is 20 nsec wide, and the address-logic signals are 100 nsec wide. A triple event, which is rejected by the system logic, is an accidental coincidence between the coincidence strobe and an unrelated address strobe. Therefore, triples can be approximated in a manner similar to the calculation of accidentals (24), where the resolving time is the sum of the strobe widths. The probability that a third unrelated address-logic pulse will overlap a coincidence strobe is approximately

$$\text{Triples} = (\text{COINCIDENCE RATE}) \times (\text{SINGLES RATE}) \times (120 \text{ nsec}) \quad (4)$$

At very high count rates, especially without septa, the accidentals rate can exceed the true coincidence rate, and a higher order of deadtime correction is required. This count rate, which is essentially an accidentals rate between coincidence events, is given as approximately

$$\text{Quadruples} = (\text{COINCIDENCE RATE}) \times (\text{ACCIDENTALS RATE}) \times (450 \text{ nsec}), \quad (5)$$

where 450 nsec is the approximate deadtime of the data collection electronics per event. Thus, while each bank pair operates independently, overlapping pairs of coincidences from any combination of bank pairs within one plane will be lost. The overlapping coincidences of concern are either trues with accidentals, or trues with trues.

In each case, deadtime is dependent on the amount of activity as either a second- or third-power function. Triple coincidences that are recorded by the PCT account for a large fraction of the deadtime due to triple

events. However, losses due to true events overlapping true events, and losses due to pileup in individual detectors, are not recorded. The measured triple events are only a fraction of the triple events, however they are dependent on the product of the singles and coincidences, and if the correct proportionality constant can be evaluated, the product of the triples and the constant would be the count loss. This approach gave a reasonable deadtime correction for most count rates, but failed at the highest rates. To add an approximation of the correction term indicated by Eq. (5), the measured deadtime losses of each scanning mode was fitted to a function of the triples involving both first- and three-halves power [Eq. (1)].

The correction equation, with one set of constants, fits a wide variety of counting conditions, including the wide range of counting rates and the wide range of singles-to-coincidence ratios that are seen in the two configurations of septa. Triple-coincidence data are available for each scan position, permitting point-by-point deadtime corrections; this can be very important for short-lived isotopes, since such scans can have significant count-rate changes over the period of a single scan. For studies in which there is little change of count rate during a scan, a single average deadtime correction would be more accurate.

**Image quality.** While various performance specifications of a PCT system provide the details of a system, the best summary of performance is the image produced by the system. In Fig. 8 are shown several images of the Derenzo phantom reconstructed with different reconstruction filters. Note, first that the finest hole pattern is resolved, second that each hole in a group is essentially the same, and third that each hole is round. These indicate, respectively, (a) that resolution is on the order of 8 mm in a complex extended object, (b) that resolution is uniform throughout the FOV, and (c) that aliasing artifacts due to insufficient sampling are imperceptible.

The carboxy(C-11) hemoglobin images were chosen because this blood-volume tracer is available at most PCT installations and most PCT systems have been tested with such scans. In a patient's image the large blood vessels of the brain act as in vivo line sources to demonstrate resolution. In these images (Fig. 11), the largest blood vessels have been suppressed to allow the lower blood volume of the tissue and smaller blood vessels to be visualized.

FDG images demonstrate the most common application. In the FDG images in Fig. 10, the convolutions of the cortical ribbon are clearly delineated; so are subcortical structures including thalamus, caudate and globus pallidus putamen complex. Both posterior and anterior limbs of the internal capsule are visualized and the basal ganglia are distinct and separated from overlying insular cortex. Also visualized are brain stem and

substructures of the cerebellum such as the cerebellar cortex, vermis, and dentate nucleus.

#### SUMMARY

The performance of the NeuroECAT is summarized best by the tables and figures in this work. In addition, note that many problem areas that are not amenable to post-acquisition corrections have been optimized in the design. The nonuniformity of image resolution, expressed as a standard deviation of the mean, is on the order of  $\pm 2$ –3% with a full range of values of about  $\pm 6$ %. The variation is not perceptible in images of the Derenzo phantom (Fig. 8). Variation of axial resolution has full range of less than 10% ( $\pm 4.3$ %) with septa. With septa retracted, single-plane variation is still less than 10%, but at the edge of interplane images the loss in axial resolution is becoming significant (28% worse than single-plane axial resolution). To put this variation in perspective, note that a similar variation of resolution is observed for a detector pair at a 45-cm separation (15.7 mm to 22.5 mm) (22) for a 24-cm FOV as compared with the NeuroECAT variation of 15.3 to 22.0 mm for a 21.8-cm FOV.

The accidental coincidences, deadtime, and scatter coincidences are amenable to post-acquisition correction schemes. Since accidentals are measured and subtracted, their primary effect is an increase of random noise in the data. Deadtime correction is based on measured data and a set of average parameters. Since such a wide range of conditions was fitted by one set of deadtime-correction factors, it is expected that deadtime-correction errors will reflect primarily the statistical error of the triple coincidences observed in individual scans. The scatter correction is less accurate, and there will be some systematic error in the estimation of the scatter, plus loss in statistical accuracy in the data. More sophisticated approaches can improve the scatter correction. In our most frequent procedure (FDG scan with septa in), the decrease in signal-to-noise ratio caused by all the above corrections (4% accidentals, 8% scatter, and 2% deadtime) would be about 9% relative to a system with no accidentals, scatter or deadtime (e.g., a 10% standard deviation would increase to 11%) with a 2–3% underestimation in scatter fraction.

We conclude that the PCT has high resolution with a high degree of uniformity throughout the FOV. In addition, the amounts of scatter, accidentals, and deadtime are low, and reasonable methods for correcting for these sources of error are available. Thus, since these errors have been minimized, quantitative measurements can be made with a high degree of confidence within the limits defined by the resolution and statistical accuracy of the particular scan. Qualitatively the performance of the system is clearly evidenced by the patient and phantom images.

#### ACKNOWLEDGMENTS

We express our appreciation to A. Ricci, G. Low, J. Miller, F. Aguillar, R. Sumida and L. Pang for technical assistance; to M. Griswald for preparing the illustrations; to Drs. J. Barrio, N. MacDonald, R. Keen, H. Padgett, J. Cook, L. McConnell, and R. Birdsall for preparation of the radiopharmaceuticals, and to A. K. Meadors for the construction of the test phantoms. This work was supported by DOE contract DE-AM03-76-SF00012, and NIH Grants R01-GM-24839-01 and P01-NS 15654-01.

#### REFERENCES

1. HOFFMAN EJ, PHELPS ME, HUANG SC, et al: A new tomograph for quantitative emission computed tomography of the brain. *IEEE Trans Nucl Sci* NS-28:99–103, 1981
2. WILLIAMS CW, CRABTREE MC, BURKE MR, et al: Design of the NeuroECAT: A high resolution, high efficiency positron tomograph for imaging the adult head or infant torso. *IEEE Trans Nucl Sci* NS-28:1736–1740, 1981
3. PHELPS ME, HOFFMAN EJ, HUANG SC, et al: ECAT: A new computerized tomographic imaging system for positron emitting radiopharmaceuticals. *J Nucl Med* 19:635–647, 1978
4. WILLIAMS CW, CRABTREE MC, BURGISS SG: Design and performance characteristics of a positron emission axial tomograph—ECAT II. *IEEE Trans Nucl Sci* NS-26:619–627, 1979
5. HOFFMAN EJ, HUANG S-C, PLUMMER D, et al: Quantitation in positron emission computed tomography: 6. Effect of nonuniform resolution. *J Comput Assist Tomogr* 6:987–999, 1982
6. HOFFMAN EJ: Comments on specifying the performance of a positron tomograph. *J Nucl Med* 23:82–83, 1982
7. HOFFMAN EJ, PHELPS ME: An analysis of some of the physical aspects of positron axial tomography. *Comput Biol Med* 6:345–360, 1976
8. DERENZO SE: Method for optimizing side shielding in positron emission tomographs and for comparing detector materials. *J Nucl Med* 21:971–977, 1980
9. HOFFMAN EJ, PHELPS ME, HUANG SC, et al: Evaluating the performance of multiplane positron tomographs designed for brain imaging. *IEEE Trans Nucl Sci* NS-29:469–473, 1982
10. HOFFMAN EJ, PHELPS ME, RICCI AR, et al: Optimization of system design parameters for emission computed tomography. Transactions of IEEE/EMBS (79CH1440-7) conference on frontiers of engineering in health care. pp 363–368, 1979 Denver, Colorado
11. BROWNE E, DAIRIKI JM, DOEBLER RE, et al: Table of isotopes. Seventh Ed., Lederer CM, Shirley VS, Eds. John Wiley and Sons, New York, 1978
12. PHELPS ME, HOFFMAN EJ, HUANG SC, et al: Effect of positron range on spatial resolution. *J Nucl Med* 16:649–652, 1975
13. DERENZO SE: Precision measurement of annihilation point spread distributions for medically important positron emitters. In *Proceedings of the 5th International Conference on Positron Annihilation*, Sendai, Japan, 1979, pp 819–823.
14. HUANG S-C, HOFFMAN EJ, PHELPS ME, et al: Quantitation in positron emission computed tomography: 2. Effects of inaccurate attenuation correction. *J Comput Assist Tomogr* 3:804–814, 1979
15. BRACEWELL RN, RIDDLE AC: Inversion of fan-beam scans in radioastronomy. *Astrophys J* 150:427–434, 1967
16. SHEPP LA, LOGAN BF: Some insights into the Fourier reconstruction of a head section. *IEEE Trans Nucl Sci* NS-21:21–43, 1974

17. CARSON RE, HUANG SC, PHELPS ME: BLD: A software system for physiological data handling and model analysis. *IEEE Proceedings of the Fifth Annual Symposium on Computer Applications in Medical Care*. (81CH1696-4) pp 561-565, 1981
18. COLSHER JG, MUEHLEHNER G: Effects of wobbling motion on image quality in positron tomography. *IEEE Trans Nucl Sci* NS-28:90-93, 1981
19. DERENZO SE, BUDINGER TF, CAHOON JL, et al: The Donner 280-Crystal high resolution positron tomograph. *IEEE Trans Nucl Sci* NS-26:2790-2793, 1979
20. IDO T, WAN CN, CASELLA V, et al: Labeled 2-deoxy-D-glucose analogs.  $^{18}\text{F}$  labeled 2-deoxy-2-fluoro-D-glucose, 2-deoxy-2-fluoro-D-mannose, and  $^{14}\text{C}$ -2-deoxy-2-fluoro-D-glucose. *J Label Compds Radiopharm XIV* 175-183, 1978
21. HUANG SC, HOFFMAN EJ, PHELPS ME, et al: Quantitation in positron emission computed tomography: 3. Effect of sampling. *J Comput Assist Tomogr* 4:819-826, 1980
22. RICCI AR, HOFFMAN EJ, PHELPS ME, et al: Emission computed tomography simulator. *IEEE Trans Nucl Sci* NS-27:479-484, 1980
23. DERENZO SE: Methods for optimizing side shielding in positron emission tomographs and for comparing detector materials. *J Nucl Med* 21:971-977, 1980
24. HOFFMAN EJ, HUANG S-C, PHELPS ME, et al: Quantitation in positron emission computed tomography: 4. Effect of accidental coincidences. *J Comput Assist Tomogr* 5:391-400, 1981
25. ALLEMAND R, GRESSET C, VACHER J: Potential advantages of a cesium fluoride scintillator for a time-of-flight positron camera. *J Nucl Med* 21:153-155, 1980
26. SNYDER DL, THOMAS LJ, TER-POGOSSIAN MM: A mathematical model for positron-emission tomography systems having time-of-flight measurements. *IEEE Trans Nucl Sci* NS-28:3575-3583, 1981
27. BROWNELL GL, CORREIA JA, ZAMENHOF RG: Positron instrumentation. In *Recent Advances in Nuclear Medicine*, Vol. 5. Lawrence JH, Budinger TF, Eds. Grune and Stratton, Inc., 1978, pp 1-49
28. PHELPS ME, HOFFMAN EJ, MULLANI NA, et al: Some performance characteristics of PETT III. In *Reconstruction tomography in diagnostic radiology and nuclear medicine*. Ter-Pogossian MM, Phelps ME, Brownell GL, et al., Eds. pp 371-391, 1977, University Park Press

### New England Chapter Society of Nuclear Medicine Technologist Section

#### 11th Annual Spring Symposium

**April 15-17, 1983**

**Sheraton Regal Inn**

**Hyannis, Massachusetts**

The 11th Annual Spring Symposium of the Technologist Section of the Society of Nuclear Medicine will be held April 15-17, 1983 at the Sheraton Regal Inn in Hyannis, Massachusetts.

The two-day scientific meetings will cover topics on nuclear medicine, NMR, echocardiography, stress and time management, and other new nuclear medicine imaging advances.

A student program will be held on Saturday, April 16th.

For more information contact:

Michael W. Plankey, CNMT  
Yale-New Haven Hospital  
Diagnostic Imaging-TE2  
20 York Street  
New Haven, CT 06504

### Hawaii Chapter Society of Nuclear Medicine 6th Annual Meeting

**May 28-30, 1983**

**Hyatt Kuilima Hotel**

**Kahuku, Oahu, Hawaii**

The Hawaii Chapter of the Society of Nuclear Medicine will hold its 6th Annual Meeting on May 28-30, 1983 at the Hyatt Kuilima Hotel located on Oahu's magnificent north shore.

Guest speakers for this year's meeting are Wil Nelp, M.D., Ernest Garcia, Ph.D., Philip Matin, M.D. and Michael Kipper, M.D.

Topics to be addressed at this Memorial Day Weekend conference include clinical and technical aspects of rotational tomography, quantification of thallium imaging, uses of monoclonal antibodies, pulmonary, bone and In-111 oxine labeled WBC imaging. Continuing Education and VOICE credits will be available for participants.

For further information contact:

Patrick McGuigan  
The Honolulu Medical Group  
Dept. of Nuclear Medicine  
550 South Beretania Street  
Honolulu, Hawaii 96813